Nanotechnol Rev 2019; 8:352–369 **DE GRUYTER**

Review Article

Jinghua Feng*, Manfred Kriechbaum, and Li (Emily) Liu*

In situ capabilities of Small Angle X-ray Scattering

https://doi.org/10.1515/ntrev-2019-0032
Received May 11, 2019; accepted Aug 22, 2019

Abstract: Small Angle X-ray Scattering (SAXS) is an ideal characterization tool to explore nanoscale systems. In order to investigate nanostructural changes of materials under realistic sample environments, it is essential to equip SAXS with diverse *in situ* capabilities based on the corresponding requirements. In this paper, we highlight the representative experimental setups and corresponding applications of five widely used *in situ* capabilities: temperature, pressure, stretching, flow-through, and electric field. Additionally, we also briefly introduce other four *in situ* techniques including humidity, high-throughput, rheology, and magnetic field.

Keywords: Small Angle X-ray Scattering, *in situ*, capability, nanoparticle, nanomaterial

1 Introduction

Small Angle X-ray Scattering (SAXS) is an analytical technique to explore material structures with relatively larger sizes (typically 1-100 nm) by detecting the scattering signals at small angle (typically 0.1°-10°) [1]. SAXS has several advantages over direct characteristic techniques such as transmission electron microscopy (TEM) and scanning electron microscope (SEM) in that: (i) it is non-destructive and post-experimental samples can be analyzed by other techniques afterwards; (ii) it rarely needs sample pretreatment; (iii) SAXS only requires a very small amount of sample; (iv) it can be either transmission mode or surface mode (GISAXS). These advantages, together with its proper probing range (1-100 nm), render SAXS an ideal tool to study nanoscale systems [2], which covers a wide range of applications including metal alloys [3–7], polymers either in solution [8–11] or as bulk materials [12–15], biological systems [16–19], porous materials [20–24], catalysts [25–29], etc. The nanoscale samples can be in any aggregation state: solid, liquid or gas; amorphous, porous or crystalline; dissolved in a solution or embedded in a solid matrix.

In many fields, it is vital to observe nanostructural changes of materials in the natural or real conditions, which motivates both synchrotron and lab SAXS to develop *in situ* capabilities. For instance, the microscopic changes of size, shape and morphology of nanoparticles with the variation of temperature can be observed via *in situ* SAXS [30–33]. *In situ* SAXS is also widely utilized to investigate the microscopic structural evolution of alloy or polymer during uniaxial or biaxial stretching, which can improve the material performances via phase transition [34–36]. Another common usage of *in situ* SAXS is to study the mechanisms and kinetics of nanoparticle nucleation and growth via flow-through device [37, 38].

Depending on the specific application, the time resolution of *in situ* SAXS can be adjusted accordingly. In the *in situ* SAXS-stress-strain experiment from Romo-Uribe's group [39], the SAXS patterns were recorded with time resolution of 10 s due to the relatively slow deformation rate of 5 mm/min. But fast nanoparticle synthesis can occur in a time span of milliseconds to a few seconds which requires relatively much higher time resolution [40]. Graceffa et al. developed a new approach which is capable of achieving a time resolution of 100 μs for *in situ* SAXS with continuous-flow mixer [41].

As it is not practical to cover all the *in situ* techniques of SAXS in one article, we pick and review nine commonly utilized *in situ* capabilities of SAXS. The experimental setups of these capabilities are briefly described and the results of some state-of-the-art applications based on these setups are reviewed and discussed.

***Corresponding Author: Jinghua Feng:** Department of Mechanical, Aerospace, and Nuclear Engineering, Rensselaer Polytechnic Institute, Troy, New York 12180, United States of America; Email: fengj3@rpi.edu
***Corresponding Author: Li (Emily) Liu:** Department of Mechanical, Aerospace, and Nuclear Engineering, Rensselaer Polytechnic Institute, Troy, New York 12180, United States of America; Email: liue@rpi.edu
Manfred Kriechbaum: Institute of Inorganic Chemistry, Graz University of Technology, Graz 8010, Austria

Open Access. © 2019 J. Feng *et al.*, published by De Gruyter. CC BY This work is licensed under the Creative Commons Attribution 4.0 License

2 *In situ* capabilities of SAXS

2.1 Temperature

The properties and behaviors of nanomaterials, such as the particle size/shape and morphology [42, 43], nanoparticle aggregation [44], are strongly dependent on synthesis temperature. For instance, the study on synthesis of gold nanoparticles (NPs) from Hatakeyama *et al.* indicates that the diameter of the most abundant NPs grows gradually from around 2 nm to 8 nm when the temperature is increased from 20 to 60°C, and the anisotropy increases with temperature increase although NPs generated at 20°C are spherical [30]. The SAXS data obtained by Ingham *et al.* revealed that the heating can induce the aggregation of the nanocrystals due to the melt and desorption of the capping ligands [31].

For many alloys, the heating and cooling rate can greatly influence the crystal grain size and phase composition, which ultimately determine the properties of the alloys. For example, Kenel *et al.* applied *in situ* SAXS to study early precipitation in Al-Cu-Mg alloys and found that the formation of η phase precipitates increases with the decrease of cooling rate [32]. Time-resolved SAXS study carried out by Deschamps *et al.* showed that increasing the heating rate can significantly decrease the precipitate density due to the influence of heating rate on nucleation rate [33].

The significant influence of temperature on the properties of nanoparticle materials makes the temperature adjustment an essential capability of *in situ* SAXS. Temperature control of the sample in SAXS can be achieved by heating or cooling.

2.1.1 Laser-driven heating

Utilizing laser-based heating and rapid cooling, Kenel *et al.* developed an approach of *in situ* SAXS combined with XRD to study alloy behavior and its influence on microstructures and properties after additive manufacturing (AM). The schematic experimental setup is shown in Figure 1. They applied two diode lasers to heat the samples. The laser spot size is ~0.2 mm^2. To heat different locations of the sample or follow sample movement, the complete setup can be translated in three dimensions. Pyrometer is used to measure the temperature of the specimen, based on which the laser can be adjusted and controlled. The samples were heated to solutionizing temperature at 474°C and held for 7 min to homogenize the microstructure. The authors obtained the Kratky plot as a function of temperature shown in Figure 2. At relatively lower temperature, the peak appearing at low q values indicates the presence of large-scale scatterers [32].

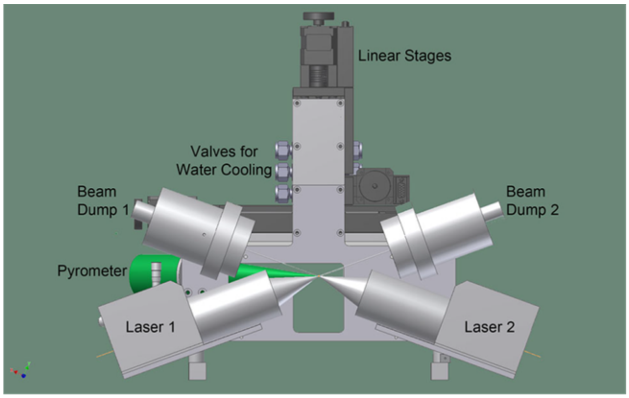

Figure 1: Setup for laser-based heating in the synchrotron radiation beamlines [32]

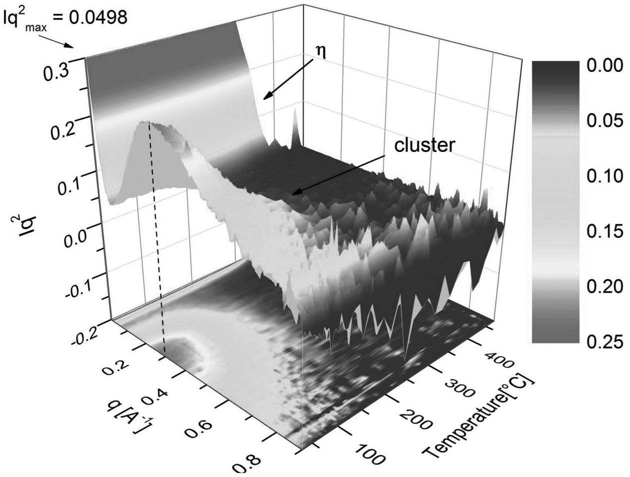

Figure 2: The Kratky plot (Iq2 versus q) as a function of temperature for the fastest quench (FQ). The Iq2 scale in the Kratky plot was set to a value of 0.3 in order to better observe the evolution for high values of the scattering vector [45]

2.1.2 Joule heating

Heat can also be generated electrically by the joule heating effect. Andreasen *et al.* designed an *in situ* cell covering temperature from around 300 K to 870 K to study size and morphology changes of nanoparticles by SAXS. The *in situ* cell is schematically presented in Figure 3. The heater el-

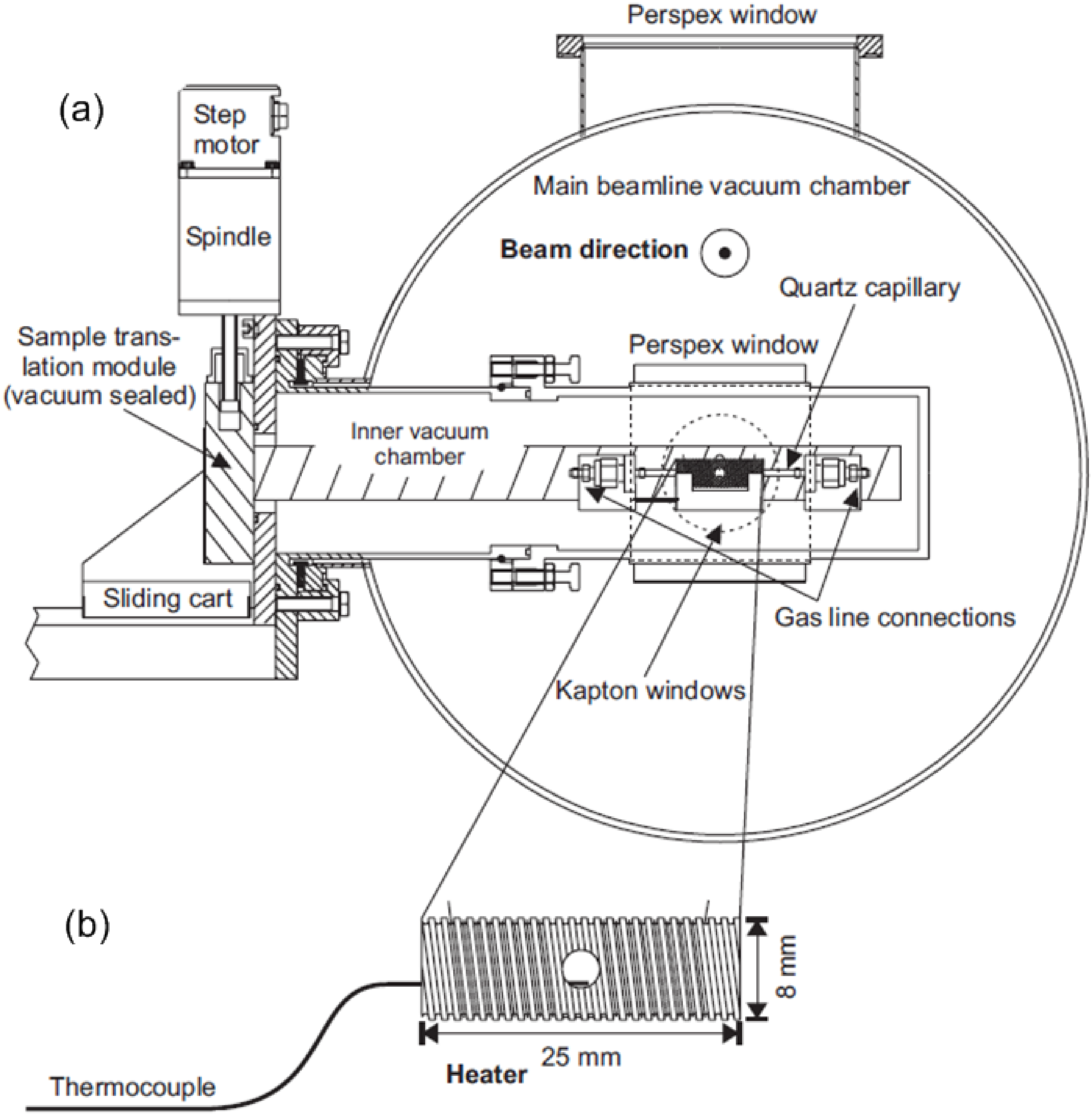

Figure 3: (a) View down the JUSIFA vacuum chamber/flight tube along the synchrotron beam direction, showing the inner vacuum chamber with the capillary micro reactor in measuring position. The entry points for gas and electrical current leads, thermocouple and vacuum pump connection are on the sample translation module in the left-hand part of the drawing. (b) Enlarged view of the heater element showing heater wire and central opening allowing beam passage. Also, the positioning of the thermocouple is shown (Reproduced with permission of the International Union of Crystallography)

ement contains a cylinder made of Macor® glass ceramic, the working temperature of which can be as high as 1070 K. The heater wire (kanthal D) with a resistance of 1.35 µΩm is wound in the 0.5 mm deep, 1 mm steep helical groove on the ceramic cylinder. A NiCr-Ni thermocouple placed 1mm below the sample volume is applied to measure the sample temperature. The temperature at the central of the heating element can reach at least 870 K. This *in situ* cell is mounted on the JUSIFA beam line at HASYLAB. The authors acquired the *in situ* SAXS data of the calcination of a hydrozincite powder heated from 350 K to 570 K at a rate of about 8 data sets per hour. Assuming a model of polydisperse spherical particles, the derived radiuses of gyration for the uncalcined and calcined sample are 118.5 ± 0.8 Å and 81.5 ± 3.1 Å, respectively [46].

The above module is a self-designed heating element. Commercial devices can also be directly used. For instance, Anton Paar DHS 1100 heating plate and chamber is applied to investigate a new mechanism for mesostructure formation of ordered mesoporous carbons (OMC): thermally induced self-assembly. During the process of thermopolymerization, DHS 1100 heating plate is used to provide a temperature between 90 and 180°C until strong reflections are observed in the *in situ* GISAXS. After that, DHS 1100 heating chamber in nitrogen atmosphere heats the samples up to 1100°C, the defined limit of this heating element. The obtained *in situ* SAXS results indicate that the structure formation of OMC systems occurs during the thermopolymerization step, but not the process of evaporation. The authors also found that the rate of structure formation is strongly dependent on the thermopolymerization temperature and the block copolymer template. Total loss of structure does not occur even when the sample is heated up to 1100°C [47].

2.1.3 Cooling by conduction

Taking advantage of the high thermal conductivity of Copper, Kenel *et al.* placed Cu sample holder under the specimen to extract heat quickly, as schematically shown in Figure 4. The cooling rate achieved based on this structure can be as high as $1.5{\cdot}10^4$ K/s [48]. The quench experiment of a commercial aluminum alloy indicates that at faster cooling rates, the clusters size is smaller while the cluster density is larger. It was also found that heterogeneous precipitates are formed more pronouncedly at lower cooling rates between 400°C and 200°C [32].

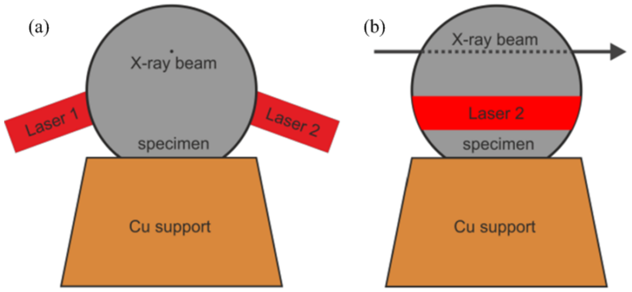

Figure 4: Measurement geometry for In situ microXRD combined with laser heating. Schematic view (a) parallel and (b) perpendicular to the incoming x-ray beam [49]

2.1.4 Cooling by Peltier effect

Albouy *et al.* used a commercial device (CT160, Deben company) equipped with a Peltier element to study self-assembly of a copolymer by freezing its aqueous solution. The lowest temperature achieved in this article is −7°C. The *in situ* SAXS experiments performed at the SWING beamline of the French SOLEIT show that micelles (aggregates of P123 molecules) can form at temperatures lower than the initial value of the CMT (critical micellar temperature), which indicates that it is not always true that self-assembly in aqueous solution of an object with weak interactions cannot take place below the CMT [50].

2.2 Pressure

Similar to temperature, pressure as another thermodynamic variable also plays an important role in synthesis of nanoparticles or supramolecular assembly of (bio)macromolecules. Unlike heating or cooling, pressure compression and decompression in a sample can be achieved with the same rate in either direction and the pressure propagates through the sample homogeneously without forming gradients. Analogous to T-jumps, p-jumps (pressurizing or depressurizing) can be conducted in both directions with the speed of sound. Soft condensed matter often undergoes thermotropic phase-transitions with temperature changes, same phase-transitions can also occur by changing pressure (barotropic phase transition) [51, 52]. That way two- dimensional phase diagrams as a function of temperature and pressure can be obtained as Figure 5 shows.

SAXS can be also used to follow the nanostructural changes of the sample with pressure in real-time. But requirements for pressure cells with *in situ* X-ray scattering techniques (SAXS, XRD) are not as simple as for T-studies. First, the cell has to be built to withstand high pressure. Second, the cell must have windows sufficiently transparent for the X-rays used. Diamond is the typical material choice for X-ray windows at high pressure due to its low electron density (Carbon: Z = 6), high hardness and toughness. The transmission for X-rays at different energies (wavelengths) for a diamond of thickness 0.5 mm is shown in Figure 6 (right). As elaborated in the following paragraphs, pressure cells for X-rays may consist of two diamonds, on which mechanical force is applied to attain a pressure of 7.5 Mbar. Or two diamond windows are integrated in a hydrostatic pressure cell in which pressure is generated by a transmitting fluid with low compressibility (up to 5 kbar).

2.2.1 Diamond-anvil cell (DAC)

A DAC consists of two opposing specially cut diamonds enclosed by a gasket and the two diamond anvils (0.2 - 0.5 carats) with a sample compressed between the polished diamond tips of small area [56]. Pressure can be monitored by a reference material with known pressure behavior like ruby and its fluorescence. The pressure is applied uniaxially and transformed into uniform hydrostatic pressure via a pressure-transmitting medium (enclosed by a gasket and the two diamond anvils) such as noble gases, hydrogen or a mixture of alcohols. Typically, a pressure of 1-2 Mbar can be reached with a maximum up to 7.5 Mbar [57]. Due to the relatively large thickness of the diamonds and consequently low transmission of X-rays, SAXS or XRD *in situ* measurements can only be carried out at synchrotron sources by selecting a short wavelength. Samples investigated by DACs are usually solid powders or crystals, but can also be liquid crystalline samples [58].

2.2.2 Hydrostatic pressure cells

The hydrostatic high pressure cell itself is machined out of stainless steel with cube dimensions of 3 x 2 x 2 cm and has two disc-shaped diamond windows with a diameter of 4 mm and a thickness of 0.75 mm each, serving as the X-ray entrance and exit windows, respectively [59]. The cell is connected to a motor-driven spindle press using water as the pressure transmitting medium. The system can be operated in automated pressure or temperature scans. The sample itself is contained in a flexible polymer-tube, closed on both ends by a teflon-piston, which is placed within the high-pressure cell. Besides slow pressure scans, fast p-jumps (<5 ms) triggered by pneumatic pressure valves, separating two reservoirs of different pressures can be applied, and the nanostructural changes in the sample can be followed by time-resolved SAXS [60, 61]. The sample in the cell can be pressurized up to moderate 3.5 kbar and above and its angular range encompasses 0° - 20° (2θ). Changing temperature in the cell can be achieved either by a circulating flow of water through copper plates or by Peltier elements between which the cell is sandwiched. The application range is widely spread from studying phase diagrams of lyotropic or thermotropic liquid crystalline systems, proteins, lipoproteins or polymers and their barotropic phase transitions [62–67]. The pressure cell can also be utilized in experiments with super-critical CO_2 [68] and in the grazing incidence mode (GISAXS) for oriented and aligned lipid systems on solid supports [69].

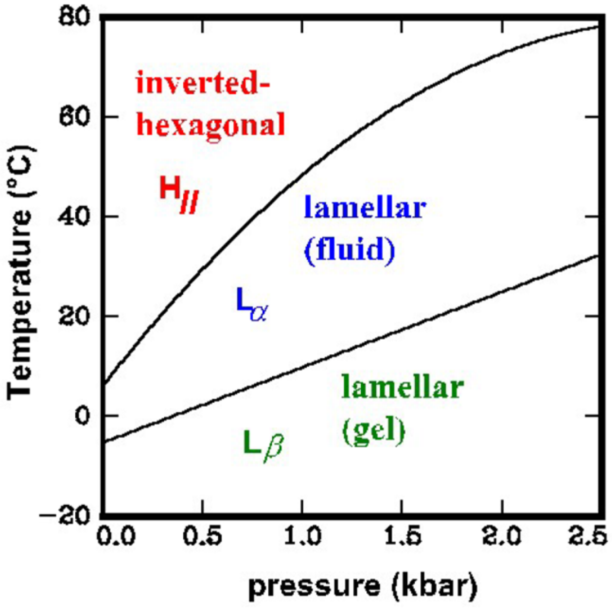

Figure 5: p/T phase-diagram of the phospholipid DOPE (Di-oleoyl-phosphatidy-ethanolamine) in excess water. Within the shown range (0 to 2.5 kbar and −20°C to 80°C) it exhibits two lamellar phases (gel and fluid) and a two-dimensional hexagonal phase [53]

2.2.3 Pressurized gas: super-critical CO_2 as with unique solvent properties

The supercritical state for carbon dioxide is experimentally easy to achieve (pc = 73.8 bar and Tc = 31.1°C) and thus can be used for *in situ* high-pressure SAXS measurements [68, 70]. A block copolymers formed by a CO_2-phobic and a CO_2-philic portion like polyvinyl acetate-b-perfluoro octyl acrylate (PVAc-b-PFOA) forms at low pressure below the critical value, micelle-like aggregates. At relatively high pressures, CO_2 becomes a good solvent for both portions, inducing the destruction of such aggregates and giving fully solvated random coil chains. By *In situ* SAXS measurements these nanostructural changes can be observed in T-scans (at constant CO_2 pressure) or at P-scans (at constant CO_2 temperature) [68].

2.2.4 Pressurized gas: CO_2 gas sorption in coal

A laboratory SAXS gas cell was used in the investigation of adsorption and swelling behavior of coal to determine the feasibility of CO_2 sequestration. CO_2 storage in appropriate geological reservoirs is considered as one possibility to decrease the amount of CO_2 in the atmosphere. The research project COALSWAD (www.coalswad.eu) dealt with

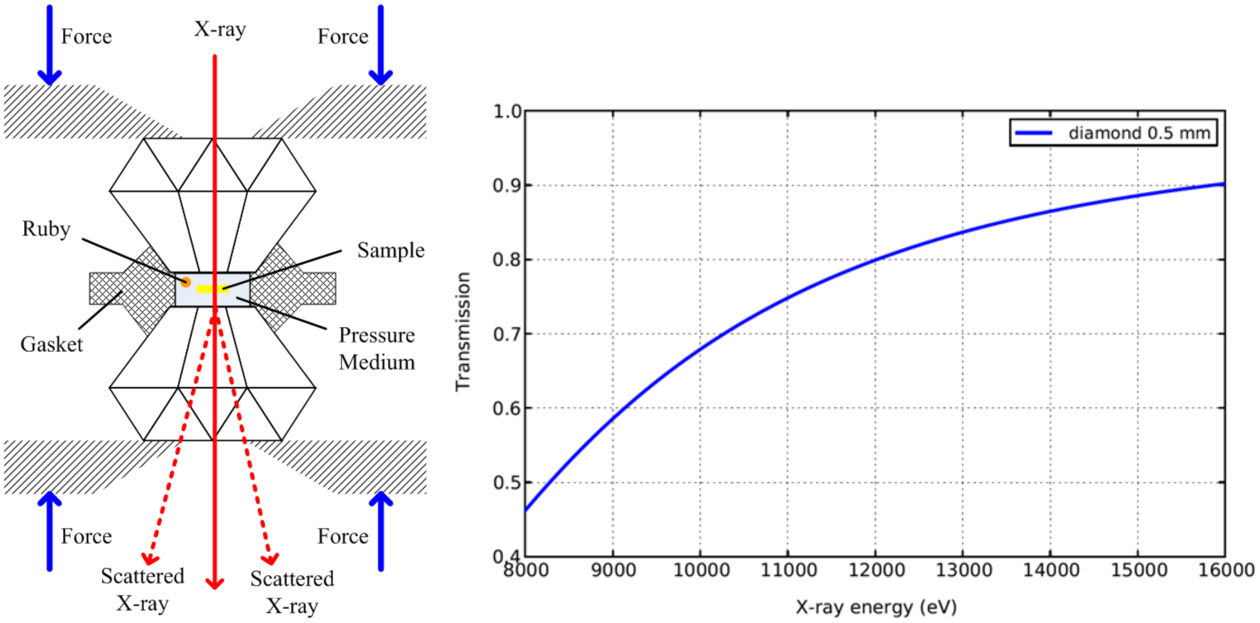

Figure 6: Left: Diamond anvil cell consisting of 2 diamonds. Hydrostatic pressure cells [54, 55]. Right: transmission of diamond of thickness 0.5 mm as a function of the energy in eV of the X-rays (which is inversely proportional to their wavelength)

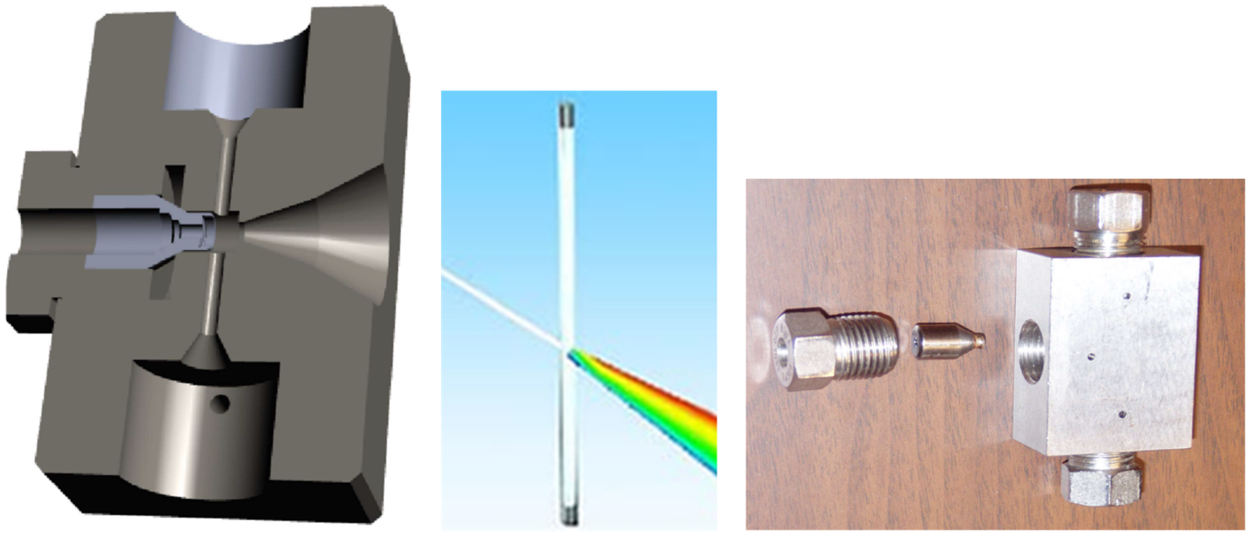

Figure 7: Horizontal cut through the hydrostatic high pressure cell (left) and the flexible polymer capillary (diameter 1.5 mm) containing the sample which fits into the central channel of the cell (middle). The beam passes from the left (entrance window) to the right (exit-window). The picture to the right shows the actual cell used at the SAXS-beamline at ELETTRA with the entrance window detached. On the right and lefts sides of the cell the high-pressure tubings for the pressure transmitting fluid (water) can be connected

the storage of CO_2 in coal seams. It focused on a comprehensive investigation of the adsorption behavior of coal and its kinetics by taking into consideration the influence of swelling properties. Results obtained by *in situ* SAXS measurements of gas sorption by different coals (up to 50 bar) show that with increasing coalification grade of coal, the degree of swelling decreases and the CO_2 adsorption capacity increases [72].

2.2.5 Pressure generated by piezo-stack actuator

The newest development for time-resolved *in situ* solution SAXS studies of kinetic processes induced by sub-ms hydrostatic pressure jumps are based on a high-force piezo-stack actuator, with which the volume of the sample can be dynamically compressed and the pressure can reach up to 1 kbar, using transparent diamond windows and an easy-

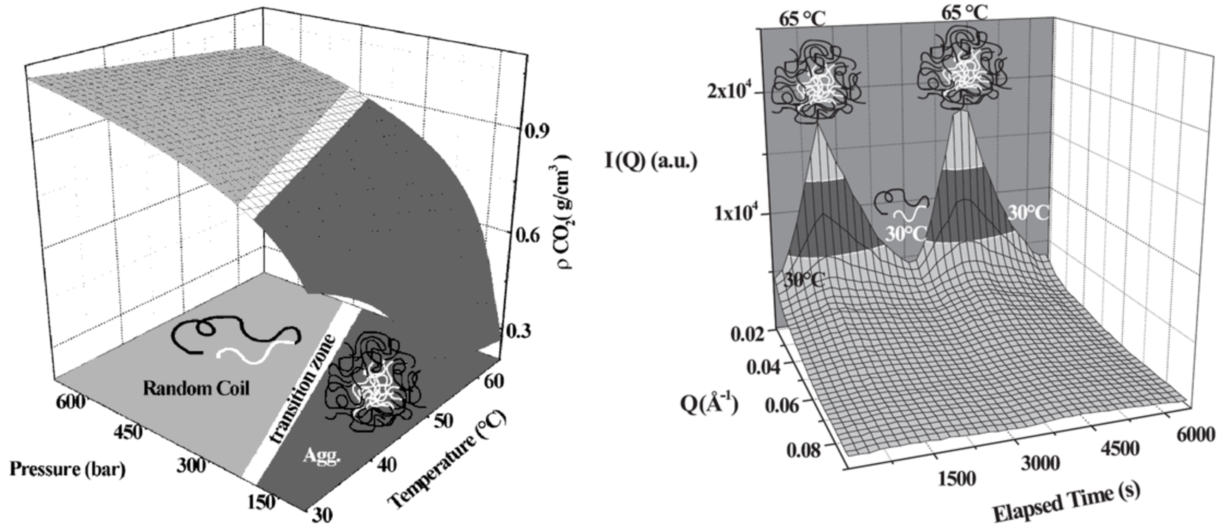

Figure 8: Left: Nano-structure (aggregates and random coils) of a the Co-Polymer (PVAc-b-PFOA) as a function of CO2 pressure, temperature and CO2 density [71]; Right: In situ scattering curves of a 7% PVAc-b-PFOA solution in CO2 at p = 250 bar at four alternate heating (up to 65°C) and cooling (down to 30°C) cycles are shown and their nanostructures depicted in the 3-D plot [68]

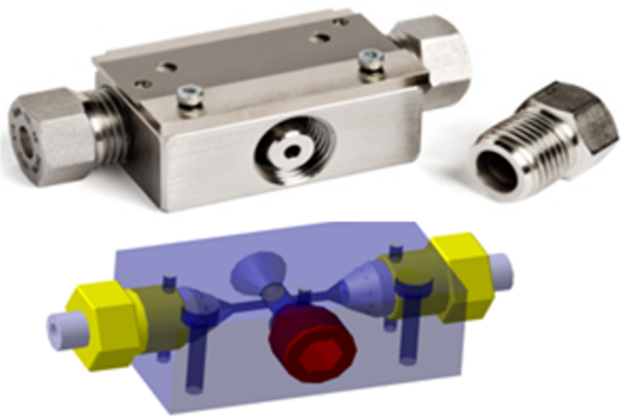

Figure 9: Picture and scheme a laboratory-SAXS gas cell used for gas sorption measurements of coal. X-rays enter from the detachable entrance-window (front). On the right and left sides the high-pressure tubes for the compressed gas are connected

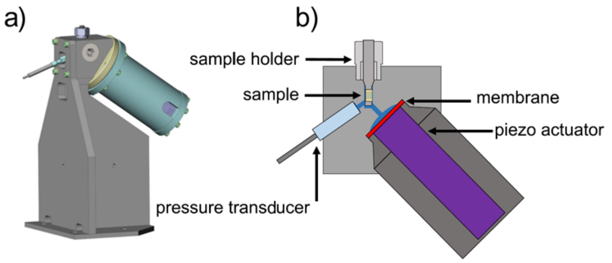

Figure 10: (a) Pressure cell mounted on the setup holder with the piezo-actuator attached; (b) Sketch of the cross section of the cell with the sample holder mounted from the top, the pressure transducer mounted from one side, and the piezo-actuator with the flexible membrane (red) mounted from the other side [73]

to-change sample capillary. The pressure in the cell can be changed in less than 1 ms and an additional temperature control offers the possibility for automated mapping of p-T phase diagrams [73].

2.3 Stretching

Besides being a typical way to evaluate mechanical properties, uniaxial or biaxial stretching is also widely applied in investigations of microscopic structural evolution of materials such as polymer [34, 35, 74–76] and alloy [77, 78], and for the improvement of material performances via phase transition [34–36]. *In situ* SAXS and wide angle x-ray scattering (WAXS) are usually combined to monitor the structural changes at lattice scale and nanoscale, respectively. The information attained at lattice scale can be used to identify the transition of crystalline phases [35], while the nanoscale information facilitates judging the appearance or extension of cavities (voids) [77, 79, 80]. Below we will review some *In situ* SAXS studies on the stretching-induced structural evolution of polymer and alloy in details.

A representative example of research on tensile deformation behavior of polymer is from Romo-Uribe's group. They applied uniaxial stretching on linear low-density polyethylene (LLDPE) and studied its nanostructure evolution by time-resolved synchrotron SAXS at the Advanced Polymer Beamline (X27C) in Brookhaven National Laboratory. Figure 11 depicts the experimental setup: a tabletop

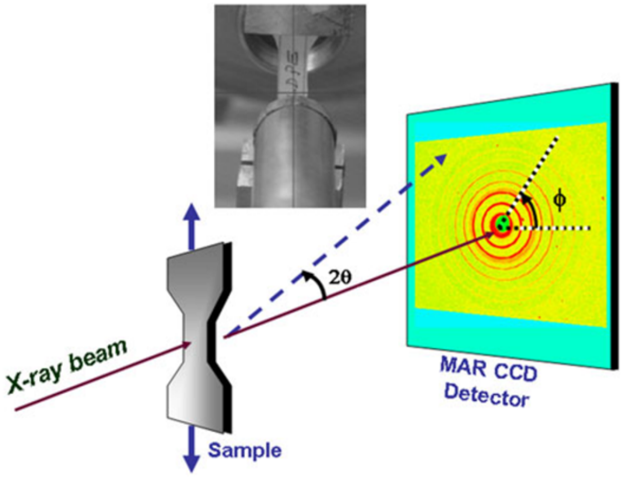

Figure 11: Experimental setup for In situ small-angle x-ray scattering (SAXS) and stress–strain experiments [39]

stretching apparatus from Instron Inc. model 4410 is utilized to stretch the sample symmetrically, ensuring the x-ray beam focus on the same spot on the sample during the deformation process. The stretching is performed at a constant speed of 5 mm/min with a 40 mm clamp-to-clamp distance. A MAR CCD of 512 × 512 pixels is applied to record SAXS patterns with time resolution of 10 s. The obtained SAXS patterns indicates that the initial LLDPE has a lamellar morphology with a long period of 21.5 nm. Flow-induced crystallization results in the increase of the long period during the initial deformation process. The lamellae are deformed toward the stretching direction between first and second yield points. In the second yield region (SYR), a gradual rotation and thinning of the off-meridional scattering reveals that a shear process is destroying the lamellae. Further deformation in SYR incurs a melting and recrystallization process in the SYR [39].

By applying SAXS/WAXS as well, Wang *et al.* investigated structural evolution in Grade 91 steel during tensile deformation at room temperature (RT) and 650°C. Grade 91 steel is an alloy containing $M_{23}C_6$ and MX precipitates, which provide the material with its high temperature creep strength. The experimental setup is schematically shown in Figure 12. The SAXS patterns were being recorded every 24 s when the alloy specimen was being continuously stretched at a constant rate of 1 µm/s, much slower than the deformation speed of polymer mentioned above. The *In situ* SAXS/WAXS was performed at Beamline 1-ID of Advanced Photon Source at Argonne National Laboratory, with a beam energy of 70 keV and beam size of 50µm × 50µm. The authors applied two ion chambers to measure the X-ray intensities before and after the sample, which is used to calculate the specimen transmission. The SAXS results indicates that for both RT and $650^{\circ}C$, the SAXS intensity does not change significantly during early deformation but begins to increase after necking occurred. The difference is that at RT, the void volume grows immediately after necking occurs at about 8.6% strain, while voids has a significant increase only after around 15% strain for temperature 650°C. The local stress concentration at the precipitate interface is alleviated by the high mobility of dislocations and thus delay void nucleation to a degree at 650°C.

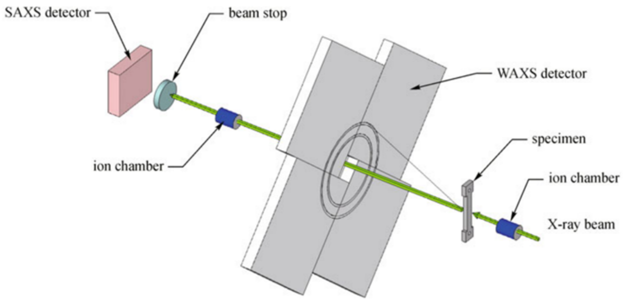

Figure 12: Scheme for simultaneous WAXS/SAXS at 1-ID beamline at APS [81]

2.4 Flow-through

In situ SAXS equipped with flow-through device is widely used to exploit the rapid formation of self-assembled structures, and study mechanisms and kinetics of nanoparticle nucleation and growth. As the parameters of the sample can be adjusted in the reaction reservoir [38] or other storage containers in the flow path [37] (not directly in the small capillary tube), the researchers can readily investigate the structural changes at different conditions such as solution pH, temperature, and concentration [82, 83].

There are typically two types of flow-through devices: stopped-flow [37, 84–86] and continuous-flow [38, 82, 87]. The stopped-flow techniques with SAXS have been applied in kinetic studies for about two decades, but with limited time resolution (~0.5 ms) and relatively higher risk of radiation damage. By reducing the dead time (time between the reaction is triggered and the first point is collected), the continuous-flow device can significantly diminish the risk of radiation damage and improve the time resolution to ~100 µs [41, 88]. Below we wish to discuss briefly some applications based on these two techniques, respectively.

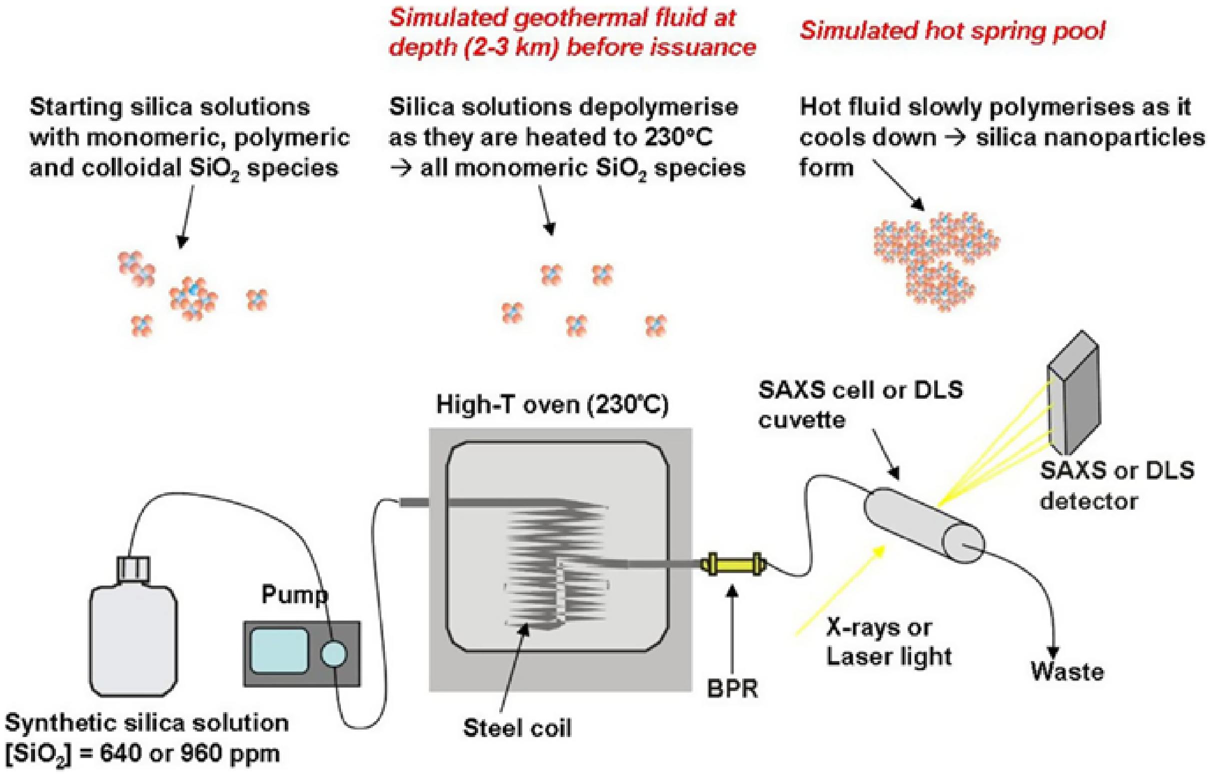

Figure 13: Schematic diagram of experimental set up to simulate a natural geothermal system where silica nanoparticles form via the fast cooling of a supersaturated monomeric silica solution (modified after Benning and Mountain, 2004). The simulator is interlinked with the In situ and real-time scattering cells and detectors [37]

2.4.1 Stopped-flow

A representative example of the application of stopped-flow technique in kinetics of nucleation and growth is from Tobler's work [37]. The authors mimicked the natural systems of silica polymerisation and silica nanoparticle formation to study the mechanism of silica nanoparticle nucleation and growth under the conditions of high temperature (230°C) and long residence time (2.5 h).

The experimental setup is schematically shown in Figure 13. The silica solution with concentration of 640 or 960 ppm in a 10 L storage bottle is pumped into a high-temperature oven by a HPLC pump. With 2.5 h residence time in the oven, the silica is completely depolymerized under the high temperature of 230°C, which is achieved by steel coil. After leaving the oven, the monomeric silica species enters the backpressure regulator (BPR), where the solution temperature drops rapidly to 80°C within 1 min. The polymerization and subsequent nucleation and growth of silica nanoparticle occurs during the rapid cooling process. To study these processes, the silica solution passes through a flow through quartz capillary which is connected to the outlet of BPR. The distance between BPR and capillary can be adjusted to achieve specific temperature (30°C for SAXS). The scattered X-ray signal of the solution sample in the capillary is monitored by SAXS detector.

The SAXS data collection is conducted every 5 min up to 3 h. The time-resolved SAXS patterns reveal that for lower concentration (660 ppm), nanoparticle with a radius of approximately 1.5 nm is observed after 60 min and the plateau of about 3.5 nm is estimated to be achieved at about 6 h. The concentration increase to 960 ppm can significantly speed up the appearance of nanoparticles, which occurs in only 10 min. It only takes 3 hours to reach the plateau of 3.5 nm. The near-Gaussian shape of the distance distribution function indicates monodisperse and spherical nanoparticles. The occurrence of some aggregates or polydispersity leads to the slight skew to the right at higher particle radius.

2.4.2 Continuous-flow

Yi *et al.* applied SAXS with continuous-flow device to investigate the growth mechanism of mesoporous silica nanoparticles (MSNs) at different solution temperature and pH [38]. The setup to monitor the dynamic growth of MSNs is schematically shown in Figure 14. The MSNs are fabricated in a 200 mL beaker, which is connected to the capillary tube by a peristaltic pump. The flow rate between the reaction reservoir and capillary tube is 0.5 mL/s. The dead time is estimated to be about 28 s based on the flow rate between the reaction reservoir and capillary tube (0.5 mL/s), pipe length (2.8 m), and pipe diameter (2.5 mm). Thus, the authors collected SAXS patterns for 2 s every 28 s. At 30°C, it took 150 min to collect about 300 patterns; while the total data acquisition at 95°C consumed only around 1 h as MSNs reaches steady state quicker at this temperature. The SAXS results suggested that increasing temperature accelerates the growth rate of MSNs as the higher temperature drives the molecule movement faster and thus escalates the contact frequency. The higher pH value also leads to the faster silica growth as the increase of hydrolysis rate of TEOS (phase transformation from liquid to solid), which is the determinant for the silica growth.

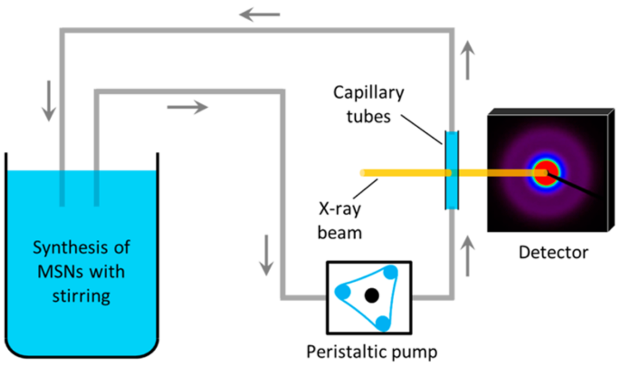

Figure 14: SAXS setup to dynamically monitor the growth of MSNs under different experimental conditions. The temperature of the reservoir for fabricating MSNs was controlled by a water bath with magnetic stirrer. The circulated reaction liquid came from the bottom of capillary tubes to the top in order to eliminate any influence of bubbles generated by the influent fluidic flow [38]

2.5 Electric field

External electric field is extensively applied in the field of nanoparticle deposition to assist in the spontaneous self-assembly of nanocomponents, which is capable of accelerating aggregation of nanoparticles [89], promoting formation of high nanoparticle density [90, 91], and modulating the size and distribution of nanoparticles [92]. Buttard *et al.* investigated the deposition of gold colloidal nanoparticle on Silicon surface and found that the curve of Au nanoparticle density versus voltage has a threshold value, at which the density has a sharp increase of two orders of magnitude [93]. Kumar *et al.* used spray pyrolysis technique to deposit gold nanoparticles on glass substrate. The Glancing incidence angle X-ray diffraction studies indicated that the higher voltage produces smaller and more uniform gold nanoparticles [92]. Qu *et al.* applied the electric field of 10-40 kV to obtain high-density FeNi nanoparticle films. The electrodeposited films possess stronger in-plane magnetic anisotropy field and higher saturation magnetization simultaneously, which are the two key factors to increase ferromagnetic resonance frequency in a wider GHz range [90, 94].

Block copolymer (BCP) is another prominent material which can be formed via the process of molecular self-assembly. But the self-assembly in the absence of external fields normally creates short range order in the BCP. The application of controlled electric field is a promising approach to induce the alignment of microdomains to generate long range order in the BCP [95, 96]. BCP may be blended with nanoparticles to achieve desired material properties. For instance, simulations from Yan *et al.* indicate that the presence of nanoparticles can impact the orientation dynamics and morphology of the lamellar microstructure in the hybrid materials under electric field [97]. Experimental from Bae et al. found that mixed microdomain orientations in BCP films under external electric field are promoted in the presence of gold nanoparticle [98].

Either direct current (DC) electric field or alternating current (AC) electric field can be applied in *In situ* SAXS based on the effects one would like to create upon the nanomaterials. For instance, Park *et al.* compared the microstructural evolution of PP/caly nanocomposites under AC and DC field. They found that AC field results in an exfoliated structure (or layer-stacking destruction) by the breakup of the charge balance while DC field leads to the alignment of silicate layers via dielectrophoretic motion [99]. Below some applications of DC and AC field will be reviewed, respectively.

2.5.1 DC electric field

Böker and Schmidt *et al.* studied the mechanisms of microdomain alignment in BCP solutions under dc electric field via *In situ* SAXS. The experimental setup is schematically shown in Figure 15. A dc voltage between 0.3 and 3.8 kV is applied across a home-built capacitor with gold electrodes, which creates a homogeneous electric field perpendicular to the direction of X-ray beam. The authors performed *In situ* SAXS experiment at the ID02 and ID2A

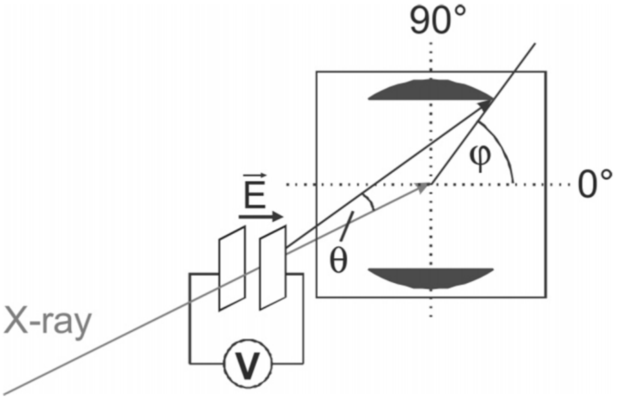

Figure 15: Experimental setup for In situ SAXS [96]

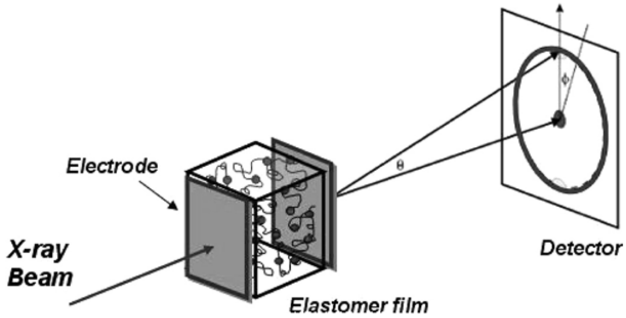

Figure 16: A schematic of an electromechanical strain measurement by using an in situ synchrotron SAXS [100]

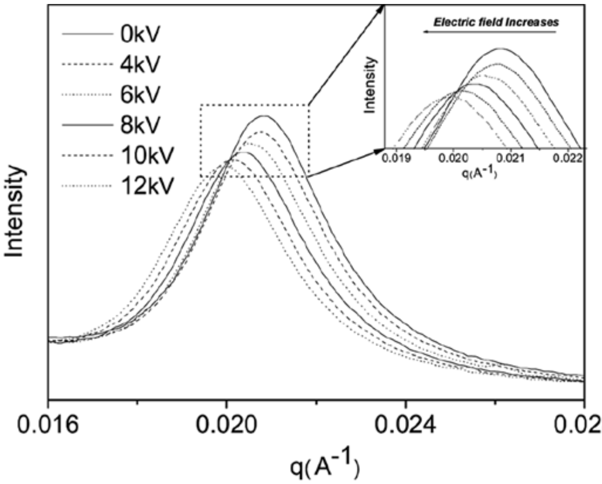

Figure 17: SAXS patterns of the SEBS gel as a function of the applied electric field [100]

beamlines at the European Synchrotron Radiation Facility. The results revealed that the process of grain boundary migration dominates in weakly segregating systems, while the rotation of entire grains is the predominant process in strongly segregated systems. They also found that the initial degree of order in BCP system can influence the microscopic mechanism greatly: in a highly ordered lamellar system, a possible pathway to reorientation is nucleation and growth of domains; in a less ordered system, grain rotation becomes an alternative pathway to realize reorientation [95, 96].

Kim *et al.* applied *in situ* synchrotron SAXS to investigate electromechanical strain responses of a poly and a maleic anhydride grafted poly dielectric elastomer gels [100]. Figure 16 shows a schematic presentation of the experimental setup. The direction of X-ray beam is perpendicular to the sample film surface and parallel to the external electric field. The authors applied a high-voltage power amplifier (Trek 10/10B) to amplify the output amplitude of the function generator (Agilent 33250A) by a factor of 1000. The adjustable high voltage (0-12 kV) is then delivered to the gel film. The synchrotron SAXS patterns of the SEBS gel during actuation is shown in Figure 17. The broader reflection peak in the absence of electric field (0 kV) indicates that the gel film has disordered micelle structure. As the electric field increases, the reflection peak is shifted to lower q ranges, which reveals the decrease of the average d-spacing in nanostructure dimension.

2.5.2 AC electric field

Paineau and Dozov *et al.* applied *in situ* SAXS to study the influence of ac electric field on the orientational degrees of the freedom of the clay platelets in both isotropic and nematic phases. Figure 18 shows the design of capillary holder and the *in situ* SAXS experimental setup. A high-frequency (700 kHz) electric field, with voltage ranging from 0 to 400 V, is applied on the sample by a pair of aluminum foil electrodes. The electrodes, rings of foil, are in direct contact with the capillary outer wall. A cushion of soft foam is used to protect the capillary tube. A highly uniform electric field, parallel to the capillary axis, can be created in the whole interelectrode area and strong up to 100 V/mm rms can be achieved in the suspension. The capillary cell was then mounted onto the experimental table of the Swing beamline. The SAXS patterns indicated that the electric field can readily align the nematic phase of beidellite clay suspensions but has no influence on the gels. The authors also observed strong field-induced orientational order in the isotropic phase of both clay suspensions [101, 102].

Dozov's group used the same electric setup shown in Figure 18 to investigate the alignment of chitin nanorods under an ac electric field via *in situ* SAXS. The obtained SAXS patterns and the effective order parameter versus

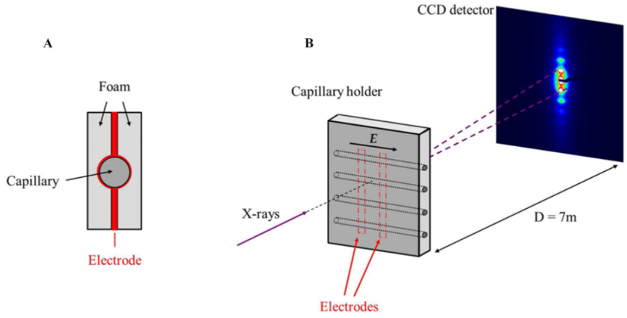

Figure 18: (A) Side view of the capillary holder; (B) Scattering geometry of the experiment [102]

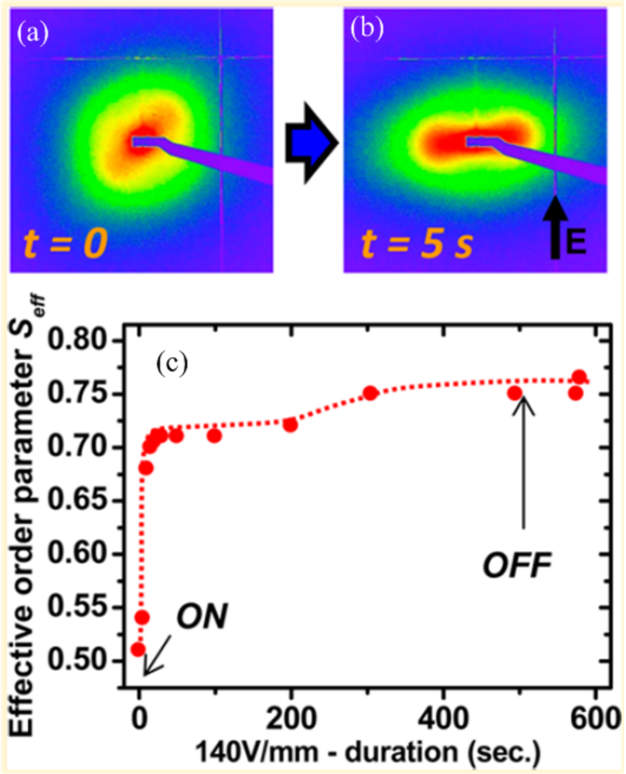

Figure 19: SAXS patterns of an anisotropic chitin nanorod- siloxane oligomers hybrid suspension in ethanol/aqueous 10^{-4} M HCl 50/50 wt %, with CCHI = 5.0 wt.%, CSi = 10.7 wt% before (a) and (b) after application of an electric field as a function of time. The direction of the field with respect to the SAXS patterns is indicated by the black arrow in (b). (c) Order parameter S inferred from I = f(ψ) traces as a function of duration of the electric field application. The two last data points were taken more than 80 s after the field was switched off. The dashed line is a guide to the eye [98]

electric field duration are displayed in Figure 19. The quick respond (at 5 s) of the anistoropic samples upon the AC electric field proves the alignment of the chitin nanoparticls along the field direction. The chitin nanorod stayed aligned after the filed is switched off (Figure 19c).

2.6 Other capabilities

In addition to the five widely applied capabilities discussed above, other *in situ* techniques that we would like to cover in this review paper include humidity, high-throughput, rheology, and magnetic field.

2.6.1 Humidity

The *in situ* control of humidity has been applied in studies of membranes via neutron or X-ray scattering for more than two decades [103–108], among which polymer electrolyte membrane (PEM) is one of the most intensively explored membranes. For instance, Jackson *et al.* reported a design of a novel *in situ* humidity chamber and simultaneously measured morphology and conductivity of a PEM under precise humidity control (Relative humidity range: 20%–95%, Relative humidity precision: 2%) [104]. Another example is from Cruz's group, who constructed an *in situ* environmental chamber that provides a humidity control with range of 0%-95% and precision of 1.5% at 30°C. The authors investigated the transient morphologies of Nafion cast film and Nafion nanofiber (a PEM) as a function of relative humidity [105].

2.6.2 High-throughput

With the rapidly growing beamline demand and ever-increasing number of samples at different solution conditions, high-throughput technique in SAXS has been developed in recent years to improve the efficiency of synchrotron beamline [109–117]. This capability is becoming extremely valuable in the biological field as the growth of sequence and genomics data significantly outpaces structural results [115]. For example, Martel *et al.* developed an automated high-throughput solution X-ray scattering data acquisition system for structural studies of protein at Stanford Synchrotron Radiation Lightsource (SSRL). They designed and constructed a compact and light sample changer for beamline 4-2 at SSRL, which can automatically deliver the sample aliquot, clean and dry the capillary, and collect the scattering data [113]. Franke *et al.* developed a modular automated SAXS data acquisition and analysis system, which was implemented and tested at the BioSAXS beamlines of European Molecular Biology Laboratory (EMBL). The authors employed the three-fold integrated networking environment (TINE) to provide reliable device communication. The sample loading, primary data reduction and further processing can be remotely controlled by software commands. Automation is conducted not only in sequence but also in parallel by taking into account the interdependencies between commands [112].

2.6.3 Rheology

In situ Rheology coupled with SAXS is commonly applied to investigate shear induced structure orientation and crystallization [118–129]. Most of these studies concentrated on the initial formation of crystallization precursor structures (*i.e.* shish-kebabs), which dictates the final morphology of the polymers [130]. As an archetypal example, Chen *et al.* studied the crystallization of isotactic polypropylene (iPP) under shear flow and Carbon Nanotubes (CNTs) via *in situ* SAXS and WAXD. The authors applied commercial Linkam CSS-450 high-temperature shearing stage at the Advanced Polymers Beamline in the National Synchrotron Light Source (NSLS), Brookhaven National Laboratory (BNL). The shear flow field and thermal history of the polymer samples can be precisely controlled via this stage. It was found that the crystallization rate of sheared CNTs/iPP nanocomposites is around 40 times as that of quiescently crystallized pure iPP. Ma *et al.* also utilized a modified Linkam CSS450 (quartz windows replaced by diamond windows for X-ray characterizations) as the flow device to explore the flow-induced shish formation in semicrystalline polymers. Their results indicate that shish are formed for a critical strain of 100 with shear rates ranging from 25 to 200 s^{-1}.

2.6.4 Magnetic field

Similar to the role that electric field plays in BCP, magnetic field is also intensively applied to produce highly oriented microstructures in BCP, which eventually determine the characteristics of materials [131–137]. For instance, Gopinadha *et al.* performed *in situ* SAXS studies of a liquid crystalline BCP under an external magnetic field, which is provided by superconducting magnet manufactured by AMI. The work shows that there is no obvious effect on order-disorder transition temperature (T_{ODT}) up to field strength of 6 T [134]. High-intensity fields (typically >4 T) restricts the wide application of magnetic field in directed self-assembly. But Gopinadha's group later utilized simple permanent magnets with a low-intensity field as small as 0.2 T to successfully produce oriented mesophases with the addition of the large grain size of labile mesogens [131].

3 Summary and outlook

In this article, the *in situ* capabilities of temperature, pressure, stretching, flow-through, and electric field for SAXS were highlighted. (1) Temperature has significant impact on the properties of nanoparticle materials. Two main heating approaches extensively applied in SAXS: laser-driven heating and Joule heating, were presented. Then cooling by conduction and Peltier effect were introduced, respectively. (2) Similarly, pressure (hydrostatic pressure to be precise) can be applied to soft matter, which nanostructure is responsive to changes of compressibility thus undergoing barotropic phase transitions or even denaturation of proteins. Alternatively, the pressure variation of the solvent CO_2 (gaseous, liquid or supercritical) can drastically alter the properties of the solute like dissolved amphiphilic polymers. The nanostructural changes can be followed by SAXS, providing a suitable sample-cell, which can cope with high pressure and that is also transparent to X-rays. (3) Uniaxial or biaxial stretching with SAXS was applied to explore structural evolution of materials at nanoscale. Stretching-induced microscopic changes of polymer and alloy were discussed. (4) *In situ* SAXS equipped with flow-through devices can be used to study the formation of self-assembled structures and kinetics of nanoparticle nucleation. Some applications of stopped-flow and continuous-flow, which are two typical flow-through devices, were provided. (5) Electric field is capable of assisting in the spontaneous self-assembly of nanocomponents and accelerating the aggregation of nanoparticles. SAXS can be combined with either direct current (DC) or alternating current (AC) electric field based on the effects one would like to create upon the nanomaterials. Besides the above five representative capabilities, the talk about other four *in situ* techniques including humidity, high-throughput, rheology, and magnetic field, was also briefly presented.

In more complicated sample environments, *in situ* SAXS equipped with a single capability is not sufficient to study the behaviors and properties of nanomaterials. Thus incorporating two or more *in situ* capabilities has become a trend for SAXS. An example where both temperature and stretching capabilities are combined is from Zhang *et al.*, who developed a radiated materials experimental module to enable *in situ* studies of radioactive specimen subject to thermo-mechanical loading at the Advanced Photon Source [138]. But SAXS has its intrinsic limitation as an analytical tool to study materials with relatively large sizes (~1-100 nm). Thus it is necessary to combine it with other techniques to study multi-scale systems. Extending SAXS simultaneously to wide-angle X-ray scattering (WAXS) is a very natural and simple choice and this has been carried out in many applications [35, 36, 76, 139, 140]. In addition, more and more non X-ray based techniques are used as complementary methods such as Fourier-transform IR spectroscopy, Raman scattering [141], UV-Vis absorption spectroscopy, etc. These combinations of techniques significantly enrich the information obtained from *in situ* experiments.

Acknowledgement: This material is based upon work supported by the U.S. Department of Energy's Office of Energy Efficiency and Renewable Energy (EERE) under the Generation 3 Concentrated Solar Power (CSP) Systems award number DE-EE0008380. This work was partially supported by Nuclear Regulatory Commission under the contract NRC-HQ-84-15-G-0018. We would like to express our great appreciation to Dr. Fallon Laliberte for her contribution to stretching capability in this paper.

References

[1] Schnablegger H., Singh Y., The SAXS guide, 2017, Anton Paar GmbH, Austria.

[2] Li T., Senesi A.J., Lee B., Small Angle X-ray Scattering for Nanoparticle Research, Chem. Rev., 2016, 116, 11128-11180.

[3] Bierska B., Lagiewka E., Pajak L., SAXS studies on Al-1.6 at.%Ag alloy and electrodeposited Cu foils and Ni-Mo alloys, J. Alloys Compd., 2004, 382, 78-83.

[4] Lima E., Bosch P., Lara V., Villarreal E., Pina C., Torres G., Martin S., Leon B., Metal corrosion in bones implanted with Zinalco - A SAXS and NMR Study, J. Biomed. Mater. Res. B, 2006, 76B, 203-210.

[5] Singh M., Sinha I., Singh A.K., Mandal R.K., LSPR and SAXS studies of starch stabilized Ag-Cu alloy nanoparticles, Colloids Surf., A, 2011, 384, 668-674.

[6] Xie R., Lu Z., Lu C.Y., Li Z.Y., Ding X.Y., Liu C.M., Characterization of nanosization of nanosized precipitates in 9Cr-ODS steels by SAYS and TEM, Acta Metall. Sin., 2016, 52, 1053-1062.

[7] Lin B., Kong L.X., Hodgson P.D., Mudie S., Hawley A., Dumee L.F., Controlled porosity and pore size of nano-porous gold by thermally assisted chemical dealloying - a SAXS study, Rsc Advances, 2017, 7, 10821-10830.

[8] Ballauff M., SAXS and SANS studies of polymer colloids, Curr. Opin. Colloid Interface Sci., 2001, 6, 132-139.

[9] Singh P.S., Ray P., Xie Z., Hoang M., Synchrotron SAXS to probe cross-linked network of polyamide 'reverse osmosis' and 'nanofiltration' membranes, J. Membr. Sci., 2012, 421, 51-59.

[10] Terao K., Morihana N., Ichikawa H., Solution SAXS measurements over a wide temperature range to determine the unperturbed chain dimensions of polystyrene and a cyclic amylose derivative, Polym. J., 2014, 46, 155-159.

[11] Cerar J., Jamnik A., Tomsic M., Testing Classical Approach to Polymer Solutions on SAXS Data of lambda-Carrageenan, kappa-Carrageenan and Methylcellulose Systems, Acta Chim. Slov., 2015, 62, 498-508.

[12] Canetti M., Bertini F., Scavia G., Porzio W., Structural investigation on bulk poly(3-hexylthiophene): Combined SAXS, WAXD, and AFM studies, Eur. Polym. J., 2009, 45, 2572-2579.

[13] Hebette C.L., Delcour J.A., Koch M.H.J., Booten K., Reynaers H.L., Crystallization and melting of inulin crystals. A small angle X-ray scattering approach (SAXS), Polimery, 2011, 56, 645-651.

[14] Xiong B.J., Lame O., Chenal J.M., Rochas C., Seguela R., Vigier G., Amorphous Phase Modulus and Micro-Macro Scale Relationship in Polyethylene via in Situ SAXS and WAXS, Macromolecules, 2015, 48, 2149-2160.

[15] Millot C., Seguela R., Lame O., Fillot L.A., Rochas C., Sotta P., Tensile Deformation of Bulk Polyamide 6 in the Preyield Strain Range. Micro-Macro Strain Relationships via in Situ SAXS and WAXS, Macromolecules, 2017, 50, 1541-1553.

[16] Kozak M., Szpotkowski K., Kozak A., Zielinski R., Wieczorek D., Gajda M.J., Domka L., The FTIR and SAXS studies of influence of a morpholine derivatives on the DMPC-based biological membrane systems, Radiat. Phys. Chem., 2009, 78, S129-S133.

[17] Brennich M.E., Round A.R., Hutin S., Online Size-exclusion and Ion-exchange Chromatography on a SAXS Beamline, Jove-J. VIS. EXP., 2017.

[18] Cheng P., Peng J.H., Zhang Z.Y., SAXS-Oriented Ensemble Refinement of Flexible Biomolecules, Biophys. J., 2017, 112, 1295-1301.

[19] Ma W.K., Chakravarthy S., Shang W.F., Irving T., SAXS: A Versatile Tool to Study Biological Macromolecules in Solution, FASEB J., 2017, 31.

[20] Pikus S., Kobylas E., SAXS studies of porous materials coated by organic layer, Fibres Text. East. Eur., 2003, 11, 70-74.

[21] Pajak L., Bierska-Piech B., Mrowiec-Bialon J., Jarzebski A.B., Diduszko R., SAXS from particle and disordered systems, Fibres Text. East. Eur., 2005, 13, 69-74.

[22] Ostafiychuk B.K., Mandzyuk V.I., Kulyk Y.O., Nagirna N.I., SAXS investigation of nanoporous structure of thermal-modified carbon materials, Nanoscale Res. Lett., 2014, 9.

[23] Folkertsma L., Zhang K.H., Czakkel O., de Boer H.L., Hempenius M.A., van den Berg A., Odijk M., Vancso G.J., Synchrotron SAXS and Impedance Spectroscopy Unveil Nanostructure Variations in Redox-Responsive Porous Membranes from Poly(ferrocenylsilane) Poly(ionic liquid)s, Macromolecules, 2017, 50, 296-302.

[24] Zienkiewicz-Strzalka M., Skibinska M., Pikus S., Small-angle X-ray scattering (SAXS) studies of the structure of mesoporous silicas, Nucl. Instrum. Meth. B, 2017, 411, 72-77.

[25] Guzman-Vargas A., Lima E., Delahay G., Coq B., Lara V., Complementary physicochemical characterization by SAXS and Xe-129 NMR spectroscopy of Fe-ZSM-5: Influence of morphology in the selective catalytic reduction of NO, Ind. Eng. Chem. Res., 2006, 45, 4163-4168.

[26] Rini A.S., Radiman S., Yarmo M.A., SAXS and XPS Characterization of Ru/Alumina Catalyst Synthesized by Microwave Irradiation Technique, Adv. Mat. Res., 2012, 364, 283-287.

[27] Valle F., Zuliani N., Marmiroli B., Amenitsch H., Taccani R., SAXS Analysis of Catalyst Degradation in High Temperature PEM Fuel Cells Subjected to Accelerated Ageing Tests, Fuel Cells, 2014, 14, 938-944.

[28] Binninger T., Fabbri E., Patru A., Garganourakis M., Han J., Abbott D.F., Sereda O., Kotz R., Menzel A., Nachtegaal M., Schmidt T.J., Electrochemical Flow-Cell Setup for In Situ X-ray Investigations I. Cell for SAXS and XAS at Synchrotron Facilities, J. Electrochem.

Soc., 2016, 163, H906-H912.

[29] Saadon N., Endud S., Bakar M.B., Lintang H.O., Roslan N., FESEM and BET studies of mesoporous catalyst SBT-15 containing Zinc porphyrin for epoxidation of limonene, J. Teknol., 2016, 78, 7-13.

[30] Hatakeyama Y., Morita T., Takahashi S., Onishi K., Nishikawa K., Synthesis of Gold Nanoparticles in Liquid Polyethylene Glycol by Sputter Deposition and Temperature Effects on their Size and Shape, Journal of Physical Chemistry C, 2011, 115, 3279-3285.

[31] Ingham B., Lim T.H., Dotzler C.J., Henning A., Toney M.F., Tilley R.D., How Nanoparticles Coalesce: An in Situ Study of Au Nanoparticle Aggregation and Grain Growth, Chem. Mater., 2011, 23, 3312-3317.

[32] Kenel C., Schloth P., Van Petegem S., Fife J., Grolimund D., Menzel A., Van Swygenhoven H., Leinenbach C., In situ synchrotron X-ray diffraction and small angle X-ray scattering studies on rapidly heated and cooled Ti-Al and Al-Cu-Mg alloys using laser-based heating, JOM, 2016, 68, 978-984.

[33] Deschamps A., Lae L., Guyot P., In situ small-angle scattering study of the precipitation kinetics in an Al-Zr-Sc alloy, Acta Mater., 2007, 55, 2775-2783.

[34] Li X.Y., Tian F., Zhou P., Yang C.M., Li X.H., Bian F.G., Wang J., In situ synchrotron small- and wide-angle X-ray study on the structural evolution of Kevlar fiber under uniaxial stretching, Rsc Advances, 2016, 6, 81552-81558.

[35] Defebvin J., Barrau S., Stoclet G., Rochas C., Lefebvre J.M., In situ SAXS/WAXS investigation of the structural evolution of poly(vinylidene fluoride) upon uniaxial stretching, Polymer, 2016, 84, 148-157.

[36] Guo H.L., Zhang Y., Xue F.F., Cai Z.W., Shang Y.R., Li J.Q., Chen Y., Wu Z.H., Jiang S.C., *In situ* synchrotron SAXS and WAXS investigations on deformation and alpha-beta transformation of uniaxial stretched poly(vinylidene fluoride), Crystengcomm, 2013, 15, 1597-1606.

[37] Tobler D.J., Benning L.G., In situ and time resolved nucleation and growth of silica nanoparticles forming under simulated geothermal conditions, Geochim. Cosmochim. Acta, 2013, 114, 156-168.

[38] Yi Z.F., Dumee L.F., Garvey C.J., Feng C.F., She F.H., Rookes J.E., Mudie S., Cahill D.M., Kong L.X., A New Insight into Growth Mechanism and Kinetics of Mesoporous Silica Nanoparticles by in Situ Small Angle X-ray Scattering, Langmuir, 2015, 31, 8478-8487.

[39] Romo-Uribe A., Manzur A., Olayo R., Synchrotron small-angle x-ray scattering study of linear low-density polyethylene under uniaxial deformation, J. Mater. Res., 2012, 27, 1351-1359.

[40] Polte J., Erler R., Thunemann A.F., Sokolov S., Ahner T.T., Rademann K., Emmerling F., Kraehnert R., Nucleation and Growth of Gold Nanoparticles Studied via in situ Small Angle X-ray Scattering at Millisecond Time Resolution, Acs Nano, 2010, 4, 1076-1082.

[41] Graceffa R., Nobrega R.P., Barrea R.A., Kathuria S.V., Chakravarthy S., Bilsel O., Irving T.C., Sub-millisecond time-resolved SAXS using a continuous-flow mixer and X-ray microbeam, J. Synchrotron Radiat., 2013, 20, 820-825.

[42] Qu Y.Q., Yang H.B., Yang N., Fan Y.Z., Zhu H.Y., Zou G.T., The effect of reaction temperature on the particle size, structure and magnetic properties of coprecipitated CoFe2O4 nanoparticles, Mater. Lett., 2006, 60, 3548-3552.

[43] Pinero S., Camero S., Blanco S., Silver nanoparticles: Influence of the temperature synthesis on the particles' morphology, Ii Colombian Congress of Electrochemistry (Cceq) and 2nd Symposium on Nanoscience and Nanotechnology (Snn), 2017, 786.

[44] Fleitas-Salazar N., Silva-Campa E., Pedroso-Santana S., Tanori J., Pedroza-Montero M.R., Riera R., Effect of temperature on the synthesis of silver nanoparticles with polyethylene glycol: new insights into the reduction mechanism, J. Nanopart. Res., 2017, 19.

[45] Schloth P., Wagner J., Fife J., Menzel A., Drezet J.-M., Van Swygenhoven H., Early precipitation during cooling of an Al-Zn-Mg-Cu alloy revealed by in situ small angle X-ray scattering, Appl. Phys. Lett., 2014, 105, 101908.

[46] Andreasen J.W., Rasmussen O., Feidenhans'l R., Rasmussen F.B., Christensen R., Molenbroek A.M., Goerigk G., An in situ cell for small-angle scattering experiments on nano-structured catalysts, J. Appl. Crystallogr., 2003, 36, 812-813.

[47] Schuster J., Kohn R., Doblinger M., Keilbach A., Amenitsch H., Bein T., In Situ SAXS Study on a New Mechanism for Mesostructure Formation of Ordered Mesoporous Carbons: Thermally Induced Self-Assembly, J. Am. Chem. Soc., 2012, 134, 11136-11145.

[48] Kenel C., Leinenbach C., Influence of cooling rate on microstructure formation during rapid solidification of binary TiAl alloys, J. Alloys Compd., 2015, 637, 242-247.

[49] Kenel C., Grolimund D., Fife J., Samson V.A., Van Petegem S., Van Swygenhoven H., Leinenbach C., Combined in situ synchrotron micro X-ray diffraction and high-speed imaging on rapidly heated and solidified Ti–48Al under additive manufacturing conditions, Scripta Mater., 2016, 114, 117-120.

[50] Albouy P.A., Deville S., Fulkar A., Hakouk K., Imperor-Clerc M., Klotz M., Liu Q., Marcellini M., Perez J., Freezing-induced self-assembly of amphiphilic molecules, Soft Matter, 2017, 13, 1759-1763.

[51] So P.T.C., Gruner S.M., Erramilli S., Pressure-Induced Topological Phase-Transitions in Membranes, Phys. Rev. Lett., 1993, 70, 3455-3458.

[52] Kulkarni C.V., Yaghmur A., Steinhart M., Kriechbaum M., Rappolt M., Effects of High Pressure on Internally Self-Assembled Lipid Nanoparticles: A Synchrotron Small-Angle X-ray Scattering (SAXS) Study, Langmuir, 2016, 32, 11907-11917.

[53] Kriechbaum M., Laggner P., States of phase transitions in biological structures, Prog. Surf. Sci., 1996, 51, 233-261.

[54] Bassett W.A., Diamond anvil cell, 50th birthday, High Pressure Research, 2009, 29, Cp5-186.

[55] Dong Z., Song Y., Novel Pressure-Induced Structural Transformations of Inorganic Nanowires, 2011, IntechOpen, London.

[56] Wang S., Meng Y.F., Ando N., Tate M., Krasnicki S., Yan C.S., Liang Q., Lai J., Mao H.K., Gruner S.M., Hemley R.J., Single-crystal CVD diamonds as small-angle X-ray scattering windows for high-pressure research, J. Appl. Crystallogr., 2012, 45, 453-457.

[57] Gebhardt R., Hanfland M., Mezouar M., Riekel C., High-pressure potato starch granule gelatinization: Synchrotron radiation Micro-SAXS/WAXS using a diamond anvil cell, Biomacromolecules, 2007, 8, 2092-2097.

[58] Czeslik C., Malessa R., Winter R., Rapp G., High pressure synchrotron X-ray diffraction studies of biological molecules using the diamond anvil technique, Nucl. Instrum. Methods Phys. Res., Sect. B, 1996, 368, 847-851.

[59] Pressl K., Kriechbaum M., Steinhart M., Laggner P., High pressure cell for small-and wide-angle x-ray scattering, Rev. Sci. Instrum., 1997, 68, 4588-4592.

[60] Steinhart M., Kriechbaum M., Pressl K., Amenitsch H., Laggner P., Bernstorff S., High-pressure instrument for small- and wide-angle x-ray scattering. II. Time-resolved experiments, Rev. Sci.

Instrum., 1999, 70, 1540-1545.

[61] Brooks N.J., Gauthe B.L.L.E., Terrill N.J., Rogers S.E., Templer R.H., Ces O., Seddon J.M., Automated high pressure cell for pressure jump x-ray diffraction, Rev. Sci. Instrum., 2010, 81.

[62] Ando N., Barstow B., Baase W.A., Fields A., Matthews B.W., Gruner S.M., Structural and thermodynamic characterization of T4 lysozyme mutants and the contribution of internal cavities to pressure denaturation, Biochemistry, 2008, 47, 11097-11109.

[63] Ando N., Chenevier P., Novak M., Tate M.W., Gruner S.M., High hydrostatic pressure small-angle X-ray scattering cell for protein solution studies featuring diamond windows and disposable sample cells, J. Appl. Crystallogr., 2008, 41, 167-175.

[64] Schroer M.A., Paulus M., Jeworrek C., Krywka C., Schmacke S., Zhai Y., Wieland D.C.F., Sahle C.J., Chimenti M., Royer C.A., Garcia-Moreno B., Tolan M., Winter R., High-Pressure SAXS Study of Folded and Unfolded Ensembles of Proteins, Biophys. J., 2010, 99, 3430-3437.

[65] Brooks N.J., Pressure effects on lipids and bio-membrane assemblies, Iucrj, 2014, 1, 470-477.

[66] Lehofer B., Golub M., Kornmueller K., Kriechbaum M., Martinez N., Nagy G., Kohlbrecher J., Amenitsch H., Peters J., Prassl R., High Hydrostatic Pressure Induces a Lipid Phase Transition and Molecular Rearrangements in Low-Density Lipoprotein Nanoparticles, Part. Part. Syst. Charact., 2018, 1800149.

[67] Winter R., Synchrotron X-ray and neutron small-angle scattering of lyotropic lipid mesophases, model biomembranes and proteins in solution at high pressure, Biochim. Biophys. Acta, Protein Struct. Mol. Enzymol., 2002, 1595, 160-184.

[68] Lo Celso F., Triolo A., Triolo F., Donato D.I., Steinhart M., Kriechbaum M., Amenitsch H., Triolo R., SAXS investigation on aggregation phenomena in supercritical CO2, Eur. Phys J. E, 2002, 8, 311-314.

[69] Rappolt M., Amenitsch H., Strancar J., Teixeira C.V., Kriechbaum M., Pabst G., Majerowicz M., Laggner P., Phospholipid mesophases at solid interfaces: *in situ* X-ray diffraction and spin-label studies, Adv. Colloid Interface Sci., 2004, 111, 63-77.

[70] Hermida-Merino D., Portale G., Fields P., Wilson R., Bassett S.P., Jennings J., Dellar M., Gommes C., Howdle S.M., Vrolijk B.C.M., Bras W., A high pressure cell for supercritical CO2 on-line chemical reactions studied with x-ray techniques, Rev. Sci. Instrum., 2014, 85.

[71] Triolo R., Lo Celso F., Triolo A., Triolo F., Steinhart M., Kriechbaum M., Amenitsch H., Critical micellisation density (CMD): a synchrotron SAXS structural study of the monomer-aggregate transition of block-copolymers in near- and super-critical fluids, Austrian Small Angle X-ray Scattering (SAXS) Beamline at ELETTRA (Annual Report 2000), 2000.

[72] Szlek A., International Conference on Carbon Reduction Technologies, CaRe Tech 2011, Polish Jurrasic Highland, Poland, September 19-22, 2011, Energy Fuels, 2012, 26, 6451-6451.

[73] Moller J., Leonardon J., Gorini J., Dattani R., Narayanan T., A subms pressure jump setup for time-resolved X-ray scattering, Rev. Sci. Instrum., 2016, 87.

[74] Stoclet G., Lefebvre J.M., Yeniad B., du Sart G.G., de Vos S., On the strain-induced structural evolution of Poly(ethylene-2,5-furanoate) upon uniaxial stretching: An *in situ* SAXS-WAXS study, Polymer, 2018, 134, 227-241.

[75] Zhang C.B., Liu G.M., Song Y., Zhao Y., Wang D.J., Structural evolution of beta - iPP during uniaxial stretching studied by *in situ* WAXS and SAXS, Polymer, 2014, 55, 6915-6923.

[76] Todorov L.V., Martins C.I., Viana J.C., In Situ WAXS/SAXS Structural Evolution Study During Uniaxial Stretching of Poly(ethylene terephthalate) Nanocomposites in the Solid State: Poly(ethylene terephthalate)/Titanium Dioxide and Poly(ethylene terephthalate)/Silica Nanocomposites, J. Appl. Polym. Sci., 2014, 131, 9.

[77] Wang L.Y., Li M.M., Almer J., Investigation of deformation and microstructural evolution in Grade 91 ferritic-martensitic steel by in situ high-energy X-rays, Acta Mater., 2014, 62, 239-249.

[78] Li M.M., Wang L.Y., Almer J.D., Dislocation evolution during tensile deformation in ferritic-martensitic steels revealed by high-energy X-rays, Acta Mater., 2014, 76, 381-393.

[79] Xiong B.J., Lame O., Chenal J.M., Rochas C., Seguela R., Vigier G., Temperature-Microstructure Mapping of the Initiation of the Plastic Deformation Processes in Polyethylene via In Situ WAXS and SAXS, Macromolecules, 2015, 48, 5267-5275.

[80] Chen R., Lu Y., Zhao J.Y., Jiang Z.Y., Men Y.F., Two-step cavitation in semi-crystalline polymer during stretching at temperature below glass transition, J. Polym. Sci., Part B: Polym. Phys., 2016, 54, 2007-2014.

[81] Wang L.Y., Li M.M., Almer J., Bieler T., Barabash R., Microstructural characterization of polycrystalline materials by synchrotron X-rays, Front. Mater. Sci., 2013, 7, 156-169.

[82] Dhasaiyan P., Prevost S., Baccile N., Prasad B.L.V., pH- and Time-Resolved in Situ SAXS Study of Self-Assembled Twisted Ribbons Formed by Elaidic Acid Sophorolipids, Langmuir, 2018, 34, 2121-2131.

[83] Baccile N., Cuvier A.S., Prevost S., Stevens C.V., Delbeke E., Berton J., Soetaert W., Van Bogaert I.N.A., Roelants S., Self-Assembly Mechanism of pH-Responsive Glycolipids: Micelles, Fibers, Vesicles, and Bilayers, Langmuir, 2016, 32, 10881-10894.

[84] Pontoni D., Narayanan T., Rennie A.R., Time-resolved SAXS study of nucleation and growth of silica colloids, Langmuir, 2002, 18, 56-59.

[85] Ortore M.G., Spinozzi F., Vilasi S., Sirangelo I., Irace G., Shukla A., Narayanan T., Sinibaldi R., Mariani P., Time-resolved small-angle x-ray scattering study of the early stage of amyloid formation of an apomyoglobin mutant, Phys. Rev. E, 2011, 84, 10.

[86] Panine P., Finet S., Weiss T.M., Narayanan T., Probing fast kinetics in complex fluids by combined rapid mixing and small-angle X-ray scattering, Adv. Colloid Interface Sci., 2006, 127, 9-18.

[87] Hu M.Z.C., Zielke J.T., Byers C.H., Lin J.S., Harris M.T., Probing the early-stage/rapid processes in hydrolysis and condensation of metal alkoxides, J. Mater. Sci., 2000, 35, 1957-1971.

[88] Grillo I., Applications of stopped-flow in SAXS and SANS, Curr. Opin. Colloid Interface Sci., 2009, 14, 402-408.

[89] Watanabe K., Tanaka E., Ishii H., Nagao D., The plasmonic properties of gold nanoparticle clusters formed via applying an AC electric field, Soft Matter, 2018, 14, 3372-3377.

[90] Ou X.L., He J., Xia Z.J., An J., Hao J.Z., He S.L., Zhao D.L., Enhancement of in-plane uniaxial magnetic anisotropy for patterned nanoparticle films fabricated by electric field-assisted deposition, Phys. B, 2017, 518, 94-98.

[91] Ou X.L., He J., Xia Z.J., Hao J.Z., Wang Y., An J., He S.L., Zhao D.L., Improvement of microwave permeability spectra in high stacking density FeNi nanoparticle films prepared by electric field-assisted deposition, Appl. Phys. A: Mater. Sci. Process., 2017, 123, 7.

[92] Kumar N., Komarala V.K., Dutta V., Deposition of gold nanoparticle films using spray pyrolysis technique: Tunability of SPR band by electric field, Phys. Status Solidi RRL, 2012, 6, 406-408.

[93] Buttard D., Oelher F., David T., Gold colloidal nanoparticle electrodeposition on a silicon surface in a uniform electric field, Nanoscale Res. Lett., 2011, 6, 8.

[94] Ou X.L., He J., Xia Z.J., An J., Hao J.Z., Yu X., He S.L., Zhao D.L., Optimized microwave magnetic characteristics for patterned FeNi nanoparticle films manufactured by electric field-assisted deposition, J. Magn. Magn. Mater., 2018, 447, 61-67.

[95] Boker A., Elbs H., Hansel H., Knoll A., Ludwigs S., Zettl H., Urban V., Abetz V., Muller A.H.E., Krausch G., Microscopic mechanisms of electric-field-induced alignment of block copolymer microdomains, Phys. Rev. Lett., 2002, 89.

[96] Schmidt K., Boker A., Zettl H., Schubert F., Hansel H., Fischer F., Weiss T.M., Abetz V., Zvelindovsky A.V., Sevink G.J.A., Krausch G., Influence of initial order on the microscopic mechanism of electric field induced alignment of block copolymer microdomains, Langmuir, 2005, 21, 11974-11980.

[97] Yan L.T., Schoberth H.G., Boker A., Lamellar microstructure and dynamic behavior of diblock copolymer/nanoparticle composites under electric fields, Soft Matter, 2010, 6, 5956-5964.

[98] Boltoeva M.Y., Dozov I., Davidson P., Antonova K., Cardoso L., Alonso B., Belamie E., Electric-Field Alignment of Chitin Nanorod-Siloxane Oligomer Reactive Suspensions, Langmuir, 2013, 29, 8208-8212.

[99] Park J.U., Choi Y.S., Cho K.S., Kim D.H., Ahn K.H., Lee S.J., Time-electric field superposition in electrically activated polypropylene/layered silicate nanocomposites, Polymer, 2006, 47, 5145-5153.

[100] Kim B., Min K., Kim J., Hong S.M., Koo C.M., The Electromechanical Properties of SEBS and SEBS-g-MA Dielectric Elastomer Gels, Mol. Cryst. Liq. Cryst., 2010, 519, 77-81.

[101] Dozov I., Paineau E., Davidson P., Antonova K., Baravian C., Bihannic I., Michot L.J., Electric-Field-Induced Perfect Anti-Nematic Order in Isotropic Aqueous Suspensions of a Natural Beidellite Clay, J. Phys. Chem. B, 2011, 115, 7751-7765.

[102] Paineau E., Dozov I., Philippe A.M., Bihannic I., Meneau F., Baravian C., Michot L.J., Davidson P., *In situ* SAXS Study of Aqueous Clay Suspensions Submitted to Alternating Current Electric Fields, J. Phys. Chem. B, 2012, 116, 13516-13524.

[103] Giahi A., Faris M.E.A., Bassereau P., Salditt T., Active membranes studied by X-ray scattering, Eur. Phys J. E, 2007, 23, 431-437.

[104] Jackson A., Beers K.M., Chen X.C., Hexemer A., Pople J.A., Kerr J.B., Balsara N.P., Design of a humidity controlled sample stage for simultaneous conductivity and synchrotron X-ray scattering measurements, Rev. Sci. Instrum., 2013, 84.

[105] Salas-de la Cruz D., Denis J.G., Griffith M.D., King D.R., Heiney P.A., Winey K.I., Environmental chamber for in situ dynamic control of temperature and relative humidity during x-ray scattering, Rev. Sci. Instrum., 2012, 83.

[106] Smith G.S., Sirota E.B., Safinya C.R., Plano R.J., Clark N.A., X-Ray Structural Studies of Freely Suspended Ordered Hydrated Dmpc Multimembrane Films, J. Chem. Phys., 1990, 92, 4519-4529.

[107] Sirota E.B., Smith G.S., Safinya C.R., Plano R.J., Clark N.A., X-Ray-Scattering Studies of Aligned, Stacked Surfactant Membranes, Science, 1988, 242, 1406-1409.

[108] Bae I., Oh K.H., Yun M., Kang M.K., Song H.H., Kim H., Nanostructured composite membrane with cross-linked sulfonated poly (arylene ether ketone)/silica for high-performance polymer electrolyte membrane fuel cells under low relative humidity, J. Membr. Sci., 2018, 549, 567-574.

[109] David G., Perez J., Combined sampler robot and high-performance liquid chromatography: a fully automated system for biological small-angle X-ray scattering experiments at the Synchrotron SOLEIL SWING beamline, J. Appl. Crystallogr., 2009, 42, 892-900.

[110] Hura G.L., Menon A.L., Hammel M., Rambo R.P., Poole F.L., Tsutakawa S.E., Jenney F.E., Classen S., Frankel K.A., Hopkins R.C., Yang S.J., Scott J.W., Dillard B.D., Adams M.W.W., Tainer J.A., Robust, high-throughput solution structural analyses by small angle X-ray scattering (SAXS), Nat. Methods, 2009, 6, 606-U683.

[111] Classen S., Rodic I., Holton J., Hura G.L., Hammel M., Tainer J.A., Software for the high-throughput collection of SAXS data using an enhanced Blu-Ice/DCS control system, J. Synchrotron Radiat., 2010, 17, 774-781.

[112] Franke D., Kikhney A.G., Svergun D.I., Automated acquisition and analysis of small angle X-ray scattering data, Nucl. Instrum. Methods Phys. Res., Sect. B, 2012, 689, 52-59.

[113] Martel A., Liu P., Weiss T.M., Niebuhr M., Tsuruta H., An integrated high-throughput data acquisition system for biological solution X-ray scattering studies, J. Synchrotron Radiat., 2012, 19, 431-434.

[114] Nielsen S.S., Moller M., Gillilan R.E., High-throughput biological small-angle X-ray scattering with a robotically loaded capillary cell, J. Appl. Crystallogr., 2012, 45, 213-223.

[115] Dyer K.N., Hammel M., Rambo R.P., Tsutakawa S.E., Rodic I., Classen S., Tainer J.A., Hura G.L., High-throughput SAXS for the characterization of biomolecules in solution: a practical approach, Methods Mol. Biol., 2014, 1091, 245-258.

[116] von Gundlach A.R., Garamus V.M., Gorniak T., Davies H.A., Reischl M., Mikut R., Hilpert K., Rosenhahn A., Small angle X-ray scattering as a high-throughput method to classify antimicrobial modes of action, Biochimica Et Biophysica Acta-Biomembranes, 2016, 1858, 918-925.

[117] Pham N., Radajewski D., Round A., Brennich M., Pernot P., Biscans B., Bonnete F., Teychene S., Coupling High Throughput Microfluidics and Small-Angle X-ray Scattering to Study Protein Crystallization from Solution, Anal. Chem., 2017, 89, 2282-2287.

[118] Portale G., Troisi E.M., Peters G.W.M., Bras W., Real-Time Fast Structuring of Polymers Using Synchrotron WAXD/SAXS Techniques, 2017, Springer International Publishing, Cham.

[119] Chen Y.H., Zhong G.J., Lei J., Li Z.M., Hsiao B.S., In Situ Synchrotron X-ray Scattering Study on Isotactic Polypropylene Crystallization under the Coexistence of Shear Flow and Carbon Nanotubes, Macromolecules, 2011, 44, 8080-8092.

[120] Keum J.K., Zuo F., Hsiao B.S., Probing the flow-induced shish-kebab structure in entangled polyethylene melts by synchrotron X-ray scattering, J. Appl. Crystallogr., 2007, 40, S48-S51.

[121] Yang L., Somani R.H., Sics I., Hsiao B.S., Kolb R., Fruitwala H., Ong C., Shear-induced crystallization precursor studies in model polyethylene blends by *in situ* rheo-SAXS and rheo-WAXD, Macromolecules, 2004, 37, 4845-4859.

[122] Nogales A., Thornley S.A., Mitchell G.R., Shear cell for in situ WAXS, SAXS, and SANS experiments on polymer melts under flow fields, Journal of Macromolecular Science-Physics, 2004, B43, 1161-1170.

[123] MacMillan S.D., Roberts K.J., Rossi A., Wells M.A., Polgreen M.C., Smith I.H., In situ small angle X-ray scattering (SAXS) studies of polymorphism with the associated crystallization of cocoa butter fat using shearing conditions, Crystal Growth & Design, 2002, 2, 221-226.

[124] Hyun K., Struth B., Meins T., Wilhelm M., *In situ* Rheo-SAXS study on shear induced alignment of liquid crystal (8CB) in the smectic phase under LAOS, Xvth International Congress on Rheology - the Society of Rheology 80th Annual Meeting, Pts 1 and 2, 2008, 1027, 1423-+.

[125] Pulamagatta B., Ostas E., Herbst F., Struth B., Binder W.H., Shear induced structure orientation in norbornene block copolymers: In situ Rheo-SAXS investigations, Eur. Polym. J., 2012, 48, 1127-1134.

[126] Liu D., Cui K.P., Huang N.D., Wang Z., Li L.B., The thermodynamic properties of flow-induced precursor of polyethylene, Science China-Chemistry, 2015, 58, 1570-1578.

[127] Troisi E.M., Portale G., Ma Z., van Drongelen M., Hermida-Merino D., Peters G.W.M., Unusual Melting Behavior in Flow Induced Crystallization of LLDPE: Effect of Pressure, Macromolecules, 2015, 48, 2551-2560.

[128] Ma Z., Balzano L., Peters G.W.M., Dissolution and Re-emergence of Flow-Induced Shish in Polyethylene with a Broad Molecular Weight Distribution, Macromolecules, 2016, 49, 2724-2730.

[129] Troisi E.M., Caelers H.J.M., Peters G.W.M., Full Characterization of Multiphase, Multimorphological Kinetics in Flow-Induced Crystallization of IPP at Elevated Pressure, Macromolecules, 2017, 50, 3869-3883.

[130] Somani R.H., Yang L., Zhu L., Hsiao B.S., Flow-induced shish-kebab precursor structures in entangled polymer melts, Polymer, 2005, 46, 8587-8623.

[131] Gopinadhan M., Choo Y., Kawabata K., Kaufman G., Feng X.D., Di X.J., Rokhlenko Y., Mahajan L.H., Ndaya D., Kasi R.M., Osuji C.O., Controlling orientational order in block copolymers using low-intensity magnetic fields, Proc. Natl. Acad. Sci. U. S. A., 2017, 114, E9437-E9444.

[132] Rokhlenko Y., Gopinadhan M., Osuji C.O., Zhang K., O'Hern C.S., Larson S.R., Gopalan P., Majewski P.W., Yager K.G., Magnetic Alignment of Block Copolymer Microdomains by Intrinsic Chain Anisotropy, Phys. Rev. Lett., 2015, 115.

[133] McCulloch B., Portale G., Bras W., Pople J.A., Hexemer A., Segalman R.A., Dynamics of Magnetic Alignment in Rod-Coil Block Copolymers, Macromolecules, 2013, 46, 4462-4471.

[134] Gopinadhan M., Majewski P.W., Choo Y., Osuji C.O., Order-Disorder Transition and Alignment Dynamics of a Block Copolymer Under High Magnetic Fields by In Situ X-Ray Scattering, Phys. Rev. Lett., 2013, 110.

[135] Majewski P.W., Gopinadhan M., Osuji C.O., Magnetic field alignment of block copolymers and polymer nanocomposites: Scalable microstructure control in functional soft materials, J. Polym. Sci., Part B: Polym. Phys., 2012, 50, 2-8.

[136] Xu B., Pinol R., Nono-Djamen M., Pensec S., Keller P., Albouy P.A., Levy D., Li M.H., Self-assembly of liquid crystal block copolymer PEG-b-smectic polymer in pure state and in dilute aqueous solution, Faraday Discuss., 2009, 143, 235-250.

[137] Hamley I.W., Castelletto V., Lu Z.B., Imrie C.T., Itoh T., Al-Hussein M., Interplay between smectic ordering and microphase separation in a series of side-group liquid-crystal block copolymers, Macromolecules, 2004, 37, 4798-4807.

[138] Zhang X., Xu C., Wang L.Y., Chen Y.R., Li M.M., Almer J.D., Benda E., Kenesei P., Mashayekhi A., Park J.S., Westferro F.J., iRadMat: A thermo-mechanical testing system for in situ high-energy X-ray characterization of radioactive specimens, Rev. Sci. Instrum., 2017, 88.

[139] Lei C.H., Xu R.J., Tian Z.Q., Huang H.H., Xie J.Y., Zhu X.Q., Stretching-Induced Uniform Micropores Formation: An in Situ SAXS/WAXS Study, Macromolecules, 2018, 51, 3433-3442.

[140] Chen X.L., Schroder J., Hauschild S., Rosenfeldt S., Dulle M., Forster S., Simultaneous SAXS/WAXS/UV-Vis Study of the Nucleation and Growth of Nanoparticles: A Test of Classical Nucleation Theory, Langmuir, 2015, 31, 11678-11691.

[141] Bras W., Koizumi S., Terrill N.J., Beyond simple small-angle X-ray scattering: developments in online complementary techniques and sample environments, IUCrJ, 2014, 1, 478-491.